Nanoscale Systems for Optical Quantum Technologies

Grant Agreement No: 712721
Start Date: 1st October 2016 - Duration: 36 months

D1.3 Optical linewidth and spin T_2 in Eu^{3+}:Y_2O_3 particles

Deliverable:	D1.3
Work package:	WP1 Nano-materials, optical micro-cavities and control systems
Task:	1.1 Y_2O_3 nanoparticles development
Lead beneficiary:	CNRS
Type:	Report
Dissemination level:	Public
Due date:	30 June 2018
Actual submission date:	30 June 2018
Author(s):	D. Serrano, A. Fossati, S. Liu, P. Goldner (CNRS-CP)

Version history

Version	Date	Author(s)	Description
V1	25/06/2018	D. Serrano, A. Fossati, S. Liu, P. Goldner (CNRS-CP)	Draft
V2	28/06/2018	D. Serrano, with comments from A. Ferrier and A. Tallaire (CNRS-CP)	Revised draft
V3	30/06/2018	D. Serrano, P. Goldner (CNRS-CP)	Submission to EC

Disclaimer

The information in this document is provided as is and no guarantee or warranty is given that the information is fit for any particular purpose. The user thereof uses the information at its sole risk and liability.

The document reflects only the authors' views and the Community is not liable for any use that may be made of the information contained therein.

Table of Contents

Deliverable Description

In the present deliverable, we describe the progress towards narrow optical and spin homogenous linewidths in Eu^{3+} doped Y_2O_3 nanoparticles with size of 100 nm, in connection with MS5. Optical homogeneous linewidths down to 25 kHz and spin coherence lifetimes greater than 1 ms have been measured in 500 nm particles, while 30 kHz and 2.6 ms were obtained on 150 nm particles. We present the two different strategies we used to obtain the smaller nanoparticles, while preserving coherence properties. Routes to further reduce dephasing mechanisms and particle sizes are discussed. These researches have been reported in three manuscripts, two of which are already published and covered in the CNRS news [1-2], and one to be submitted (Appendix).

Context

The benefits in terms of single ion detection, qubit readout and 2-qubit gates which are expected to be achieved from the coupling of rare-earth nanoparticles to optical micro-cavities (WP2) strongly rely on the optical and spin coherence lifetimes of the nanoparticles. Furthermore, as described in deliverable D1.1, the particle size can limit the maximum Purcell factor which can be achieved in the cavities through scattering losses. For losses below 10 ppm, particle diameter of no more than 50 nm is required in the case of Eu^{3+}, taking into account its optical transition wavelength (580.883 nm vac. or 516.098 THz). In the case of Er^{3+}, the transition wavelength is around 1.5 μm and 100 nm particles can be used to reach the same loss level. Obtaining long coherence lifetimes (T_2) is a challenging task when scaling down in size because of increased surface to volume ratio and potentially higher defect and impurity concentrations linked to chemical synthesis methods. Indeed, significant drops in the optical and spin coherence properties is often observed in nano-materials [3-4]. In this context, pioneer work carried out at CNRS-CP demonstrated that chemically synthesized rare-earth doped nanocrystals, aggregated in micron size particles, could present narrow optical homogeneous linewidth (Γ_h) down to 86 kHz [5]. From this starting point, NanOQTech efforts at CNRS-CP have focused on synthesizing non-aggregated nanoparticles with long optical coherence lifetimes, measuring their spin properties for the first time, and developing methods to decrease the nanoparticles' size while preserving optical and spin coherent properties.

Methods

Optical and spin coherence lifetimes were measured by photon echo and all-optical spin echo techniques for ensembles of poly-crystalline Y_2O_3: Eu^{3+} nanoparticles synthesized by homogeneous precipitation, with different average sizes and similar crystalline grain sizes around 100 nm. The Eu^{3+} concentration was set to 0.3% which provided enough absorption without introducing too much strain in the host [6]. The chemical route goes as follows: in a Teflon reactor, urea and 7.5 mM of yttrium and europium nitrates are mixed with 800 mL of solvent and heated at 85 °C for 24 h. The urea concentration is chosen depending on the desired final particle size. In particular, 0.3 mol L^{-1} yields large ~400-500 nm particles while a 3 mol L^{-1} concentration gives ~150 nm particles. Urea decomposition in the heated reactor leads to the precipitation of amorphous yttrium carbonates (YOC) particles which are then washed with water and ethanol, dried at 80 °C for 2 days and annealed under air at 1200 °C for 6 h to finally obtain Y_2O_3 crystalline

particles. A post treatment under a pure oxygen plasma generated in a home-made microwave system operating at 2.45 GHz and 900 W is performed after synthesis for 6 minutes at 1 mbar total pressure. The reactive oxygen species produced in the plasma aim at reacting with the surface of the nanoparticles and removing any residual impurities left following the synthesis process. Scanning electron microscopy (SEM) and transmission electron microscopy (TEM) analysis are used to confirm particle sizes and morphology. The crystal structure and crystalline grain sizes are determined by X-ray diffraction (Panalytical XPert Pro).
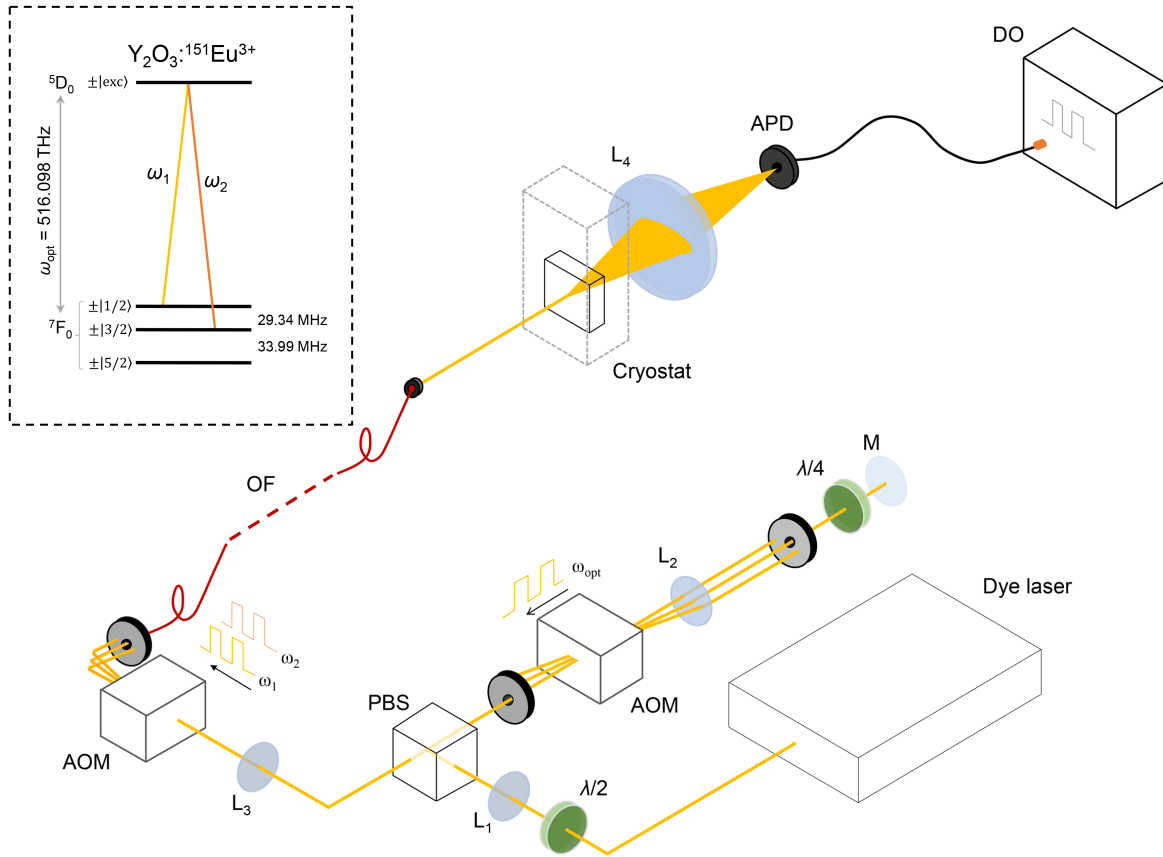

Figure 1: Experimental setup. PBS states for polarizing beam splitter, AOM for acousto-optic modulator, M for mirror, L for lens, OF for optical fiber, APD for avalanche photo diode and DO for digital oscilloscope. The first AOM, in double pass configuration was used in all experiments to modulate the laser intensity in order to create pulse sequences. The second AOM, in single pass configuration, was used in spin echo experiments for generating two-color pulses with frequencies ω_1 and ω_2. **Inset:** energy level scheme of $^{151}Eu^{3+}$ ions in Y_2O_3.

Spectroscopic experiments were carried out with the samples in form of powders placed between two glass plates with a copper spacer ($\sim$500 µm thickness) within a He bath cryostat (Janis SVT-200). The excitation is provided by a Sirah Matisse DS laser with a linewidth of approximately 150 kHz in resonance with Eu^{3+} $^7F_0$-$^5D_0$ transition (**Figure 1, inset**). The laser beam is first sent through a double pass acousto-optic modulator (AOM) with a central frequency of 200 MHz followed by a single pass AOM with a center frequency of 110 MHz. Both AOMs were driven by an arbitrary waveform generator (AWG) with 625 MS/s sampling rate. The single pass AOM is used to create two-color pulses for spin echo experiments performed on the $\pm|1/2\rangle - \pm|3/2\rangle$ ground state nuclear spin transition of $^{151}Eu^{3+}$ (I=5/2). The first diffraction order is coupled to a single-mode

fiber in order to ensure high spatial overlap between the two colors. For photon echoes, this AOM is simply kept in continuous mode. The fiber output is focused onto the sample within the cryostat with a 75 mm focal length lens. Scattered light through the sample is collected by a series of lenses from the rear side of the cryostat to be finally focused on an avalanche photo diode (APD). A scheme of the experimental setup is displayed in **Figure 1**. The sample temperature was monitored with a temperature sensor attached to the sample holder with thermally conducting grease and tuned by controlling the helium gas flow and the pressure inside the cryostat. Magnetic fields perpendicular to the laser beam propagation axis could be applied using Helmholtz coils sitting outside the cryostat.

Figure 2 displays the photon echo (**Fig. 2a**) and spin echo (**Fig. 2b**) sequences. The principle of both sequences is the same: a first pulse, labelled 'excitation', drives a rare-earth ion ensemble into a coherent superposition. This superposition is created between the optical ground and excited states in the case of photon echo experiments (at the optical frequency ω_{opt} = 516.018 THz) and between two ground state spin levels in spin echo experiments. In the latter case, this is done by an all-optical approach using two-color laser pulses as shown in **Fig. 1 inset** (with $|\omega_1 - \omega_2|$ = 29.34 MHz, the $^{151}Eu^{3+}$ spin transition frequency). This initial coherence quickly decays due to the frequency-dependent phase evolution of each ion. After a certain delay 'τ', a rephasing or π pulse is applied, which effectively reverses the phase evolution so that, at the same delay after the second pulse, or equivalently, '2τ' after the first pulse, the ion ensemble has rephased. In the optical transition, the rephasing gives rise to photon echo emission, here detected by interference between the echo and a frequency shifted pulse (heterodyne pulse). In the spin echo case, the rephased spin coherence is first converted to optical coherence by an optical pulse at ω_2, and then detected as a beating between the transferred coherence at ω_1 and the transfer pulse itself at ω_2 (see ref. [2] for more details).
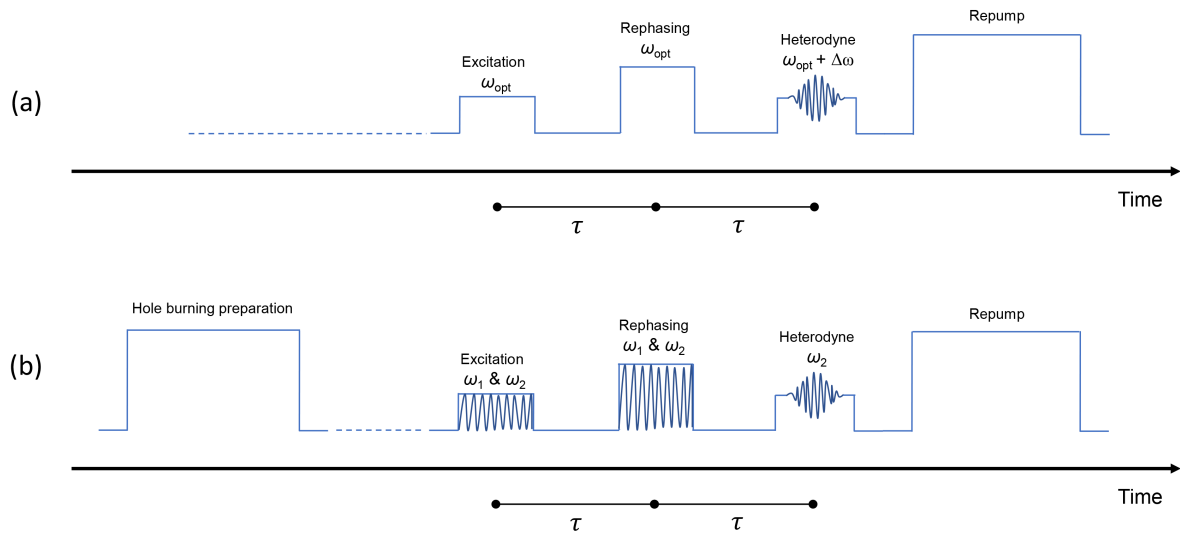
Figure 2: (a) Two-pulse photon echo sequence. Optical pulses at frequency ω_{opt} = 516.018 THz are used to create and rephase a superposition state created in the ion ensemble. The emitted photon echo is detected by interference with a frequency-shifted heterodyne pulse. The sequence ends with a series of pulses (labelled 'repump') to reset population equilibrium in the ground state spin levels. (b) Two-pulse all-optical spin echo sequence. This sequence is preceded by spin polarization to the $\pm|1/2\rangle$ level, carried out by spectral hole burning. Two-color pulses at frequencies ω_1 and ω_2 are then used to create and rephase spin coherences and a single frequency pulse at ω_2 is sent for spin coherence detection. The sequence ends in the same way as the photon echo one, with a series of pulses which set the ground state population back to equilibrium.

As 'τ' increases the number of ions which are efficiently rephased decreases due do decoherence, i.e. random phase shifts, leading to a decrease in echo amplitude E which in a general way can be written as [7]:

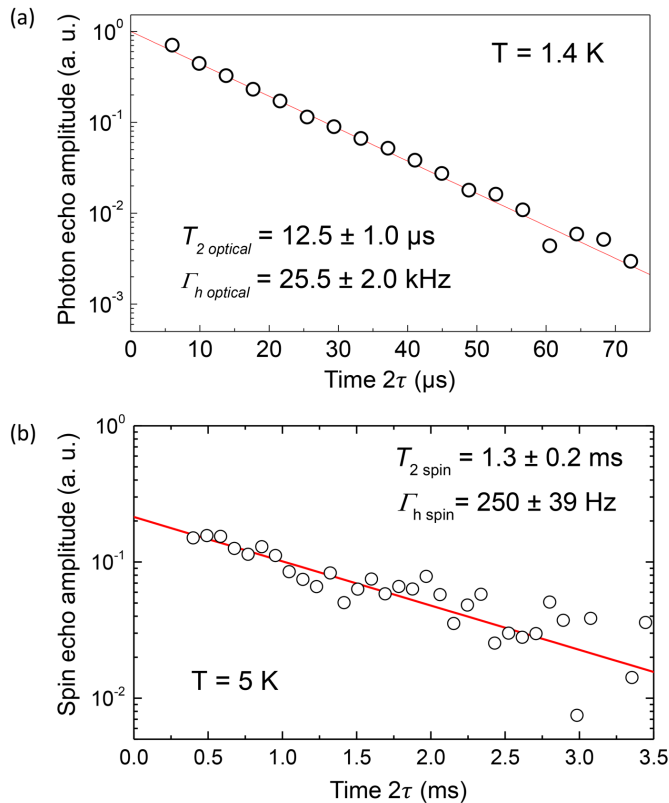$$E(\tau) = E_0 \exp\left(-\frac{2\tau}{T_2}\right)^x$$

As it will be shown in next sections, in our experiments, most photon echo and spin echo decays are exponential ($x = 1$), therefore, T_2 values could be derived from decay curves by single exponential fit.

Optical and spin homogeneous linewidths in Eu^{3+} doped Y_2O_3 nanoparticles

Large nanoparticles (~400 nm)

Exhaustive photon echo and spin echo investigations were first carried out in 400-nm diameter nanoparticles. The detail of these studies is given in refs [1-2]. An optical T_2 of 7 μs was measured, cor-responding to Γ_h = 45 kHz [1], a value comparable to those obtained in some bulk materials [8-9], highlighting the high crystalline quality of the particles. We further improved coherence lifetimes by applying a post-synthesis treatment under oxygen plasma to the particles. As an example, a recent result is displayed in **Fig. 3a**, yielding Γ_h = 25 kHz. Optimization of the treatment and more advanced spectroscopic investigations to understand its effects are currently in progress.

Spin echoes measured for the first time in rare-earth doped nanoparticles appeared to be in the millisecond range [2]. At zero field, spin T_2 is equal to 1.3 ms, which corresponds to a homogeneous linewidth Γ_h = 250 Hz (**Fig. 3b**). This homogeneous linewidth could be reduced down to 110 Hz (T_2 = 2.9 ms, **Fig. 4a**) by applying a weak external magnetic field, which is explained by a decrease in the magnetic dipole-dipole interaction (see [2] for further details). Interestingly, from [1-2] studies, it can be concluded that spin T_2 is much more preserved than the optical T_2 in the nanoparticles. Therefore,

Figure 3: (a) Photon echo decay from 400-nm-diameter particles. (b) Spin echo decay from 400-nm-diameter particles. Spin T_2 was here measured for the first time and found equal to 1.3 ms.

the difference compared to bulk values is less than one order of magnitude for the spin T_2 [7-8] , 1.3 vs. 12 ms, while larger than two orders of magnitude for optical T_2, 0.007 vs 1 ms. This behavior suggests that the nature of the dephasing mechanisms responsible for the optical and spin T_2 values in the nanoparticles are different, being associated to electric effects, either in the particles surface or in the volume, for the optical coherence [1], and to paramagnetic defects in the case of spin coherence [2]. The precise nature of these defects is still unclear and under investigation. We expect that further reduction of defects and impurities in the particles will improve both optical and spin coherence values to a large extent (see Discussion below).
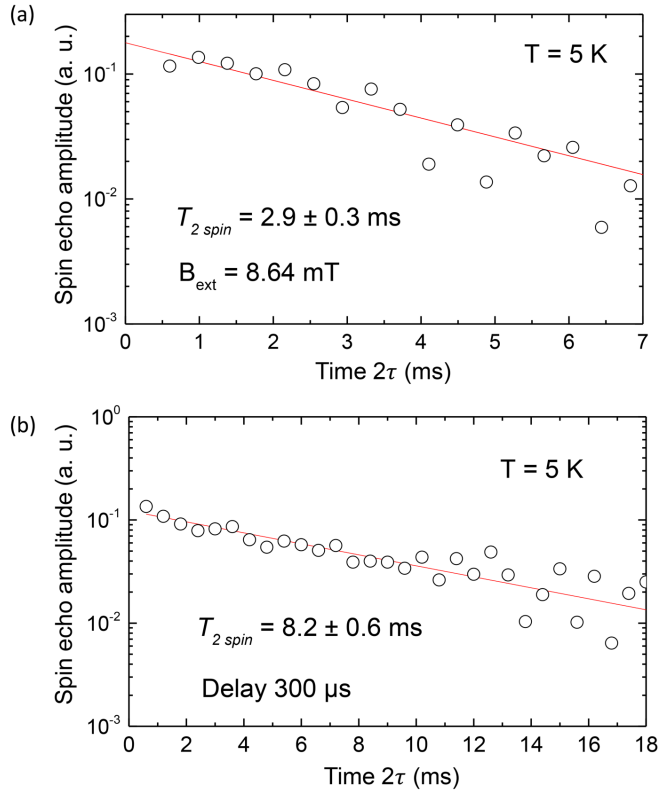
Spin coherence lifetime extension was also achieved in the nanoparticles by dynamical decoupling [12]. This sequence was here carried out fully-optically for the first time [2]. In our scheme, standard RF pulses were replaced by two-color pulses as the ones depicted in **Figure 2b** for excitation and rephasing. The best dynamical decoupling result is displayed in **Fig. 4b**, obtained with a CPMG sequence [13] with 62 optical 2-color π pulses and a π -pulse separation of 300 μs.

Figure 4: (a) Spin echo extension under an 8.6 mT external magnetic field. (b) Spin echo extension by all-optical dynamical decoupling.

Towards smaller nanoparticles

As explained in the introduction, the particle size needs to be sufficiently small to reduce scattering and ensure an efficient coupling between rare-earth doped nanoparticles and optical micro-cavities. In this context, two different strategies were pursued in order to obtain nanoparticles in the 100-nm diameter range and below. Both of them have so far given encouraging results in terms of optical and spin coherence lifetimes.

Chemical synthesis

The homogeneous precipitation chemical route allows for morphology and size distribution control. As mentioned above, the amount of urea introduced with the precursors determines the final particle size. In particular, a concentration of 3 mol L^{-1} yields Y_2O_3 nanoparticles with an average diameter between 100 and 150 nm (**Figure 5a**). Further size reduction can also be achieved by changing the solvent from water to a mixture of ethanol, butanol and water (ratio 1:2:2). In the latter case, with 3 mol L^{-1} of urea, one can get particles down to 80 nm diameter. The main difficulty of this approach

resides in the need for a high-temperature annealing step (~ 1200 °C), which causes particles to sinter and aggregate. Crystallization of the amorphous carbonates (YOC) to Y_2O_3 can be achieved at 700°C, but previous investigations showed that higher temperatures are required to fully cure defects and ensure narrow optical linewidths [6]. In the present investigation, aggregation has been limited to some extent by performing annealing in two steps, first at lower temperature (~800°C) to initiate crystallization and then around 1200 °C to cure remaining defects. Despite this, aggregation still occurs as displayed in **Figure 5a,** although the number of aggregates is small compared to that of dispersed single particles. This is important in terms of cavity applications, where single particles are targeted.
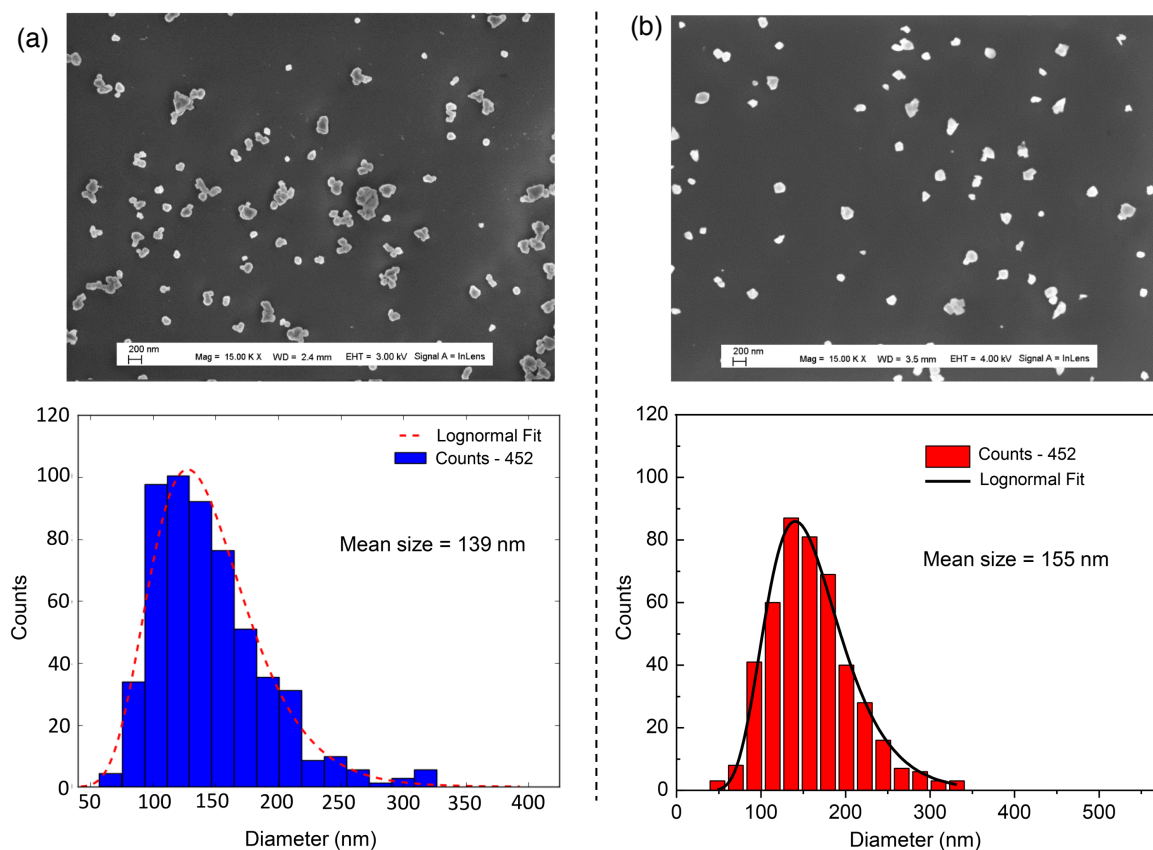
Figure 5: (a) SEM image and size histogram of Y_2O_3:0.3% Eu^{3+} nanoparticles synthesized with 3M urea after 1200 °C annealing. Large size aggregates (>350 nm) are not accounted for in the histogram which represents the size distribution of single particles. (b) SEM image and size histogram of Y_2O_3:0.3% Eu^{3+} nanoparticles obtained by wet chemical etching from standard 400-nm-diameter particles. The etching approach avoids aggregation.

Wet chemical etching

Particle size reduction by wet chemical etching was investigated as an alternative to direct chemical synthesis in order to avoid aggregation issues. The etching was performed as follows: first, Y_2O_3:Eu^{3+} nanoparticles with average size 400 nm were synthesized with annealing at 1200 °C; then they were etched in acetic acid solutions of 50 wt.% acid content (8.53 mol L^{-1}). A weak acid (pKa = 4.76 at 25 °C) was chosen to obtain low etching rates, allowing control over the size reduction process. A deep analysis of the particles sizes, morphologies and inner structure after etching evidenced a progressive size reduction of the particles on average with no effect on the crystalline grain sizes. The

etching mechanism was indeed found to preferentially act on the particles' grain boundaries. Indeed, after several hours of etching some of the poly-crystalline particles appear reduced to a single crystalline grain. The etching rate was found equal to 7.6×10^6 nm^3 h^{-1} and the activation energy of the material was estimated at 0.51 eV. Full details are given in the unpublished manuscript in Appendix. An issue with this approach is the very large material loss that occurs during etching.

Optical inhomogeneous linewidths
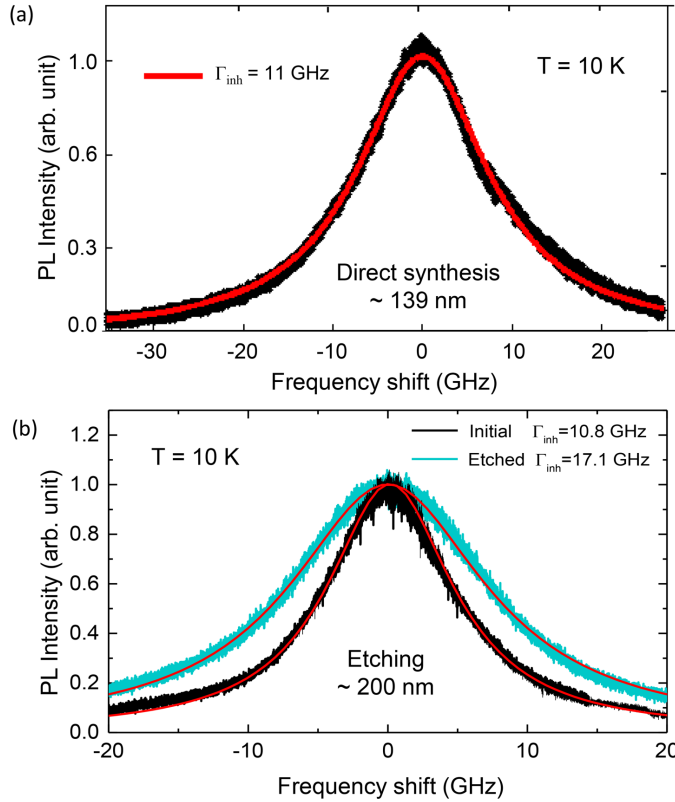
Optical inhomogeneous linewidths were recorded at low temperature (~10 K) by monitoring the $^5D_0$-$^7F_2$ fluorescence while scanning the laser through the $^7F_0 \rightarrow {}^5D_0$ transition. Particles directly synthesized with 140 nm average diameter showed values around 11 GHz (**Fig. 6a**), as expected for particles annealed at 1200°C [6]. After etching, nevertheless, a clear broadening was observed in all measured samples, as in the example shown in **Fig. 6b**.

Figure 6: Optical inhomogeneous linewidths. (a) Synthesized particles, with average diameter of 140 nm, annealed at 1200 °C. (b) Etched particles compared to the initial 400-nm-diameter ones. Solid lines: Lorentzian fits.

As displayed in **Figure 6**, line shapes can be described by Lorentzian functions both in etched and non-etched particles. This indicates that point defects are the source of the inhomogeneous broadening [14]. In non-etched particles, broadening is dominated by Eu^{3+} ions themselves, highlighting the low content of other defects in these materials [6]. Upon etching, strain is not expected to change in the crystalline grains as their size is not noticeably changed during the process. We therefore attribute the additional broadening observed in etched particles to an increase in point defects at the surface of the crystalline grains.

Optical and spin T_2 in small particles

The optical echo decays recorded from the samples in **Figure 5** are displayed in **Figure 7a and 7b**. Etched particles show a single exponential decay yielding a T_2 of 9.3 μs (Γ_h=34 kHz). Compared to the initial particles before etching (Γ_h=25 kHz), the broadening due to etching is less than 10 kHz despite the large broadening of the inhomogeneous line (**Fig. 6a**). This constitutes a very encouraging result for this approach since a volume reduction of 95% from the initial particles is achieved with only small degradation of the optical

coherence lifetime. Photon echo decays recorded from particles directly synthesized at small sizes present bi-exponential character after oxygen-plasma treatment, with a fast decay component (with a decay constant of the order of 3 µs) and a long component in the 10 µs range, displayed in **Fig. 7b,** that could correspond to ions in specific environments (e.g. well crystallized particles) that is not clearly identified yet. Spin echo signals were also measured in this sample (**Fig. 7c**). Spin T_2 in the millisecond range was found although, in contrast to spin echo measurements carried out in large particles, the decay is clearly modulated as previously observed in Y_2O_3:Eu^{3+} transparent ceramics [10]. It was therefore fitted with a function of the form:

$$E(\tau) = E_0 \exp\left(-\frac{2\tau}{T_2}\right)\left[1 + m\cos^2\left(\frac{\omega\tau}{2}\right)\right]$$

These very recent results are also very encouraging given the long optical and spin T_2 measured for the as-synthesized 140 nm particles.
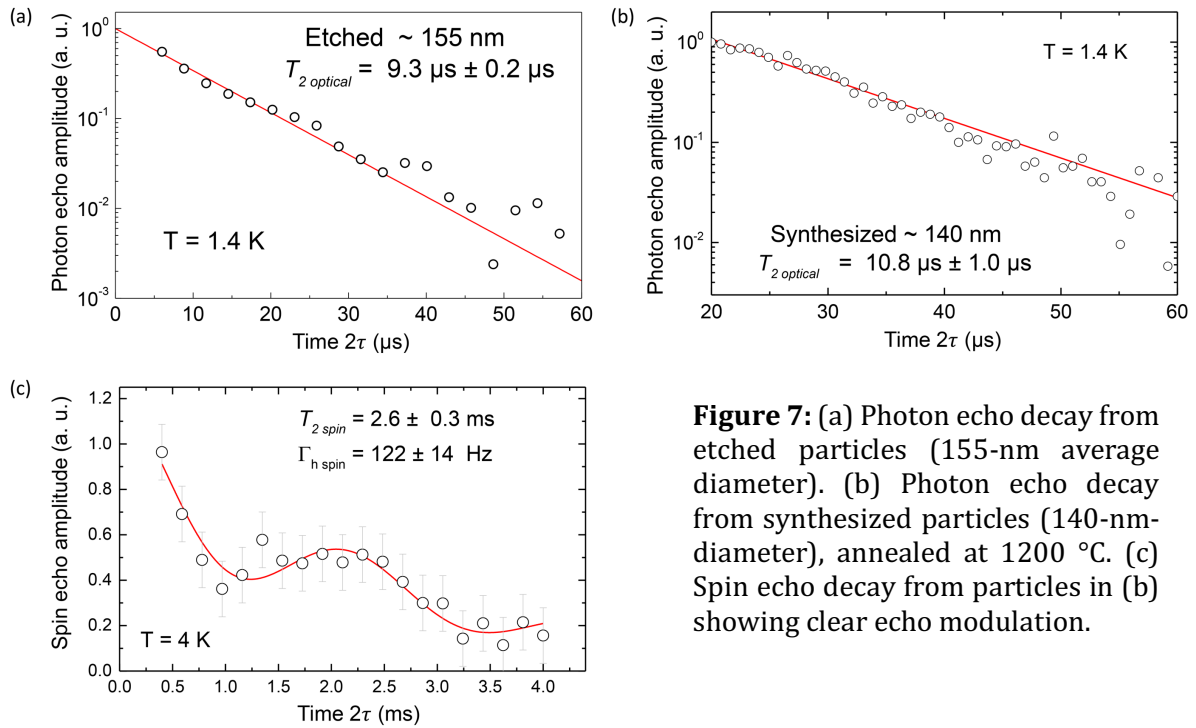
Figure 7: (a) Photon echo decay from etched particles (155-nm average diameter). (b) Photon echo decay from synthesized particles (140-nm-diameter), annealed at 1200 °C. (c) Spin echo decay from particles in (b) showing clear echo modulation.

Discussion and perspectives

The long optical and spin coherence lifetimes measured in 400 and 150 nm Eu^{3+}:Y_2O_3 particles are unique in the solid state. In particular, the ms range spin T_2 are the longest reported for optically addressable spins in any nano-materials. They are comparable to values found in bulk materials and the additional dephasing is likely to be limited by magnetic impurities or defects. We currently study ways to reduce them through improved syntheses and post-treatments. Importantly, we showed that spin T_2 can be extended by all-optical dynamical decoupling, although strong light scattering and particle random orientations cause a large spread in Rabi frequencies, limiting in turn the efficiency of the technique. In a single particle or ion, these issues disappear and we expect

T_2 extensions by orders of magnitude using a combination of dynamical decoupling and magnetic field induced clock transitions, as shown in bulk crystals [15]. This is a key point for NanOQTech's WP2 since qubits are defined within the ground state spin transition.

Optical transitions show a large broadening compared to the best bulk materials. Our detailed spectroscopic studies attribute it to dephasing related to low frequency, structural fluctuations (Two Level Systems) and electric field fluctuations due to charges or dipoles on the particle surface. Their contributions at 1.4 K is about 10 kHz (TLS) and 10-30 kHz (surface effects) and could be reduced in improved materials, a topic we are currently investigating through synthesis optimization and post-treatments. We note that the TLS contribution could be reduced below 1 kHz (i.e. in the range of bulk homogeneous linewidths) by cooling the samples to 50 mK temperatures. The current optical linewidths should be however narrow enough for the ion-ion interactions planned in WP2.

The investigations performed in Y_2O_3 nanoparticles of different sizes suggest that the coherence properties depend primarily on the crystal grain size rather than on the particle size. For example, optical and spin T_2 coherences are preserved to a large extent when the particle size is reduced from 400 nm to around 150 nm by etching or direct synthesis (95% volume reduction). In this process however, the grain size, on the order of 100 nm, does not vary. Indeed, the main difference between large and small particles is that the first ones are composed by a larger amount of crystalline grains.

Smaller particles, in the range of 100 nm and below, are currently synthesized and studied. Preliminary results indicate that in particles of 100 nm average size, optical and spin T_2 of 6.5 µs and 2.6 ms have been observed. This is promising with respect to our goals on materials as stated in MS5: 30 kHz optical homogeneous linewidth and 1 ms spin T_2 in particles < 100 nm. While this size is small enough to couple Er^{3+} ions to a micro-cavity without detrimental losses, Eu^{3+} doped particles require smaller sizes, about 50 nm. We plan to produce these materials by etching of larger particles that can be annealed at high temperatures, while direct synthesis could produce strong sintering and aggregation at the annealing step.

Conclusion

In this deliverable we report the results of the optical and spin coherence investigations carried out in Y_2O_3:Eu^{3+} nanoparticles at CNRS-CP. Milestone values of around 30 kHz optical homogeneous linewidth and > 1 ms spin T_2 have been achieved in ~150 nm particles although a further size reduction below 100 nm is required for efficient coupling to optical micro-cavities, with current researches focused on this goal. These researches have so far yielded three journal articles [1-2] and Appendix.

Bibliography

[1]   J. G. Bartholomew, K. de Oliveira Lima, A. Ferrier, P. Goldner, "Optical Line Width Broadening Mechanisms at the 10 kHz Level in Eu^{3+}:Y_2O_3 Nanoparticles", *Nano Lett.*, 17 (2), 778-787 (2017).

[2]   D. Serrano, J. Karlsson, A. Fossati, A. Ferrier, P. Goldner, "All-optical control of long-lived nuclear spins in rare-earth doped nanoparticles", *Nat. Commun.*, 9 (1), 2127 (2018).

[3]   T. Lutz *et al.*, "Effects of mechanical processing and annealing on optical coherence properties of Er^{3+}:$LiNbO_3$ powders", *J. Lumin.*, 191, 2-12 (2017).

[4]   H. S. Knowles, D. M. Kara, M. Atatüre, "Observing bulk diamond spin coherence in high-purity nanodiamonds", *Nat. Mater.* 13 (1), 21-25 (2014).

[5]   A. Perrot *et al.*, "Narrow Optical Homogeneous Linewidths in Rare Earth Doped Nanocrystals", *Phys. Rev. Lett.* 111 (20), 203601 (2013).

[6]   K. de Oliveira Lima, R. Rocha Gonçalves, D. Giaume, A. Ferrier, P. Goldner, "Influence of defects on sub-Å optical linewidths in Eu^{3+}: Y_2O_3 particles", *J. Lumin.*, 168, 276-282 (2015).

[7]   W. B. Mims, "Phase Memory in Electron Spin Echoes, Lattice Relaxation Effects in CaO_4: Er, Ce, Mn", *Phys. Rev.* 168 (2), 370-389 (1968).

[8]   G. P. Flinn, K. W. Jang, J. Ganem, M. L. Jones, R. S. Meltzer, R. Macfarlane, "Sample-dependent optical dephasing in bulk crystalline samples of Y_2O_3:Eu^{3+}", *Phys. Rev. B* 49 (9), 5821-5827 (1994).

[9]   A. Ferrier *et al.*, "Narrow inhomogeneous and homogeneous optical linewidths in a rare earth doped transparent ceramic", *Phys. Rev. B* 87 (4), 041102 (2013).

[10]   J. Karlsson, N. Kunkel, A. Ikesue, A. Ferrier, P. Goldner, "Nuclear spin coherence properties of $^{151}Eu^{3+}$ and $^{153}Eu^{3+}$ in a Y_2O_3 transparent ceramic", *J. Phys. Condens. Matter* 29 (12), 125501 (2017).

[11]   A. Arcangeli, M. Lovrić, B. Tumino, A. Ferrier, P. Goldner, "Spectroscopy and coherence lifetime extension of hyperfine transitions in $^{151}Eu^{3+}$:Y_2SiO_5", *Phys. Rev. B* 89 (18), 184305 (2014).

[12]   M. F. Pascual-Winter, R.-C. Tongning, T. Chanelière, J.-L. Le Gouët, "Spin coherence lifetime extension in Tm^{3+}:YAG through dynamical decoupling", *Phys. Rev. B* 86 (18), 184301 (2012).

[13]   S. Meiboom et D. Gill, "Modified Spin-Echo Method for Measuring Nuclear Relaxation Times", *Rev. Sci. Instrum.* 29 (8), 688-691 (1958).

[14]   A. M. Stoneham, "The theory of the strain broadened line shapes of spin resonance and optical zero phonon lines", *Proc. Phys. Soc.* 89 (4), 909 (1966).

[15]   M. Zhong *et al.*, "Optically addressable nuclear spins in a solid with a six-hour coherence time", *Nature* 517 (7533), 177-180 (2015).

Appendix

"Controlled size reduction of rare earth doped nanoparticles for optical quantum technologies"

Shuping Liu[1], Diana Serrano[1], Alexandre Fossati[1], Alexandre Tallaire[1], Alban Ferrier[1,2], and Philippe Goldner[1]

[1]Chimie ParisTech, PSL University, CNRS, Institut de Recherche de Chimie Paris, F-75005 Paris, France

[2]Sorbonne Université , Faculté des Sciences et Ingénierie, UFR 933, F-75005 Paris, France

Controlled size reduction of rare earth doped nanoparticles for optical quantum technologies

Shuping Liu,*,† Diana Serrano,*,† Alexandre Fossati,† Alexandre Tallaire,† Alban
Ferrier,†,‡ and Philippe Goldner†

†*Chimie ParisTech, PSL University, CNRS, Institut de Recherche de Chimie Paris,
F-75005 Paris, France*

‡*Sorbonne Université , Faculté des Sciences et Ingénierie, UFR 933, F-75005 Paris, France*

E-mail: shuping.liu@chimieparistech.psl.eu; diana.serrano@chimieparistech.psl.eu

Abstract

Rare earth doped nanoscale particles with sub-wavelength size can be coupled to optical micro- or nano-cavities, enabling efficient single ion readout and control, a key requirement for quantum processors and high fidelity single ion quantum memories. However, producing small size particles with good dispersion and exploitable optical coherence properties is highly challenging by most synthesis and nano-fabrication methods. We report here on the wet chemical etching of polycrystalline Eu^{3+}:Y_2O_3 nanoparticles, which are promising materials for quantum storage and processing. The impact of parameters such as etching time and temperature on the particles size and morphology is investigated, showing that etching proceeds by attacking first grain boundaries and then detached grains. We demonstrate that a controlled size reduction can be achieved by this approach, while maintaining long optical coherence lifetimes (T_2): the 12.5 μs and 9.3 μs values obtained for 430 nm initial particles and 150 nm etched particles respectively, reveal a broadening of only 10 kHz after etching. These values are

moreover the longest T_2 values reported for any nanoparticles. These results open the way to new rare earth based nanoscale quantum technologies.

Keywords

Y$_2$O$_3$, rare earth nanoparticles, chemical etching, optical coherence, quantum technologies.

1 Introduction

Trivalent rare earths (REs) doped into a host material are attractive for multiple applications since they can present extremely sharp optical absorption and emission lines without photobleaching. Therefore, rare-earth materials have been intensively investigated and widely exploited for multiple photonic and optoelectronics applications including solid-state lasers[1], fiber-based optical amplifiers[2], phosphors[3] and luminescent solar concentrators[4]. Moreover, the development of rare-earth based nano-materials has further extended the range of useful outputs to fields such as bio-imaging[5,6], photodynamic therapy (PDT)[6], lighting[7] and security[8]. In the last years, rare-earth doped crystals have also raised a strong interest in the field of quantum information processing and communication, triggered by their potential in optical quantum technologies[9–12]. Because of the shielding of 4f electrons by the outer filled 5s and 5p electron shells, the optical transitions of RE ions can exhibit very narrow optical and spin homogeneous linewidths (Γ_{h}) at cryogenic temperatures, or equivalently, long optical and spin coherence lifetimes $T_2 = (\pi \Gamma_{\mathrm{h}})^{-1}$. Ions of interest include Yb^{3+}[13], Eu^{3+}[14], Er^{3+}[15], Nd^{3+}[16], Pr^{3+}[17] and Tm^{3+}[18] doped into crystals such as Y$_2$SiO$_5$[13–17], YAG[18] or YVO$_4$[19]. The longest optical coherence lifetime in a solid state system, $T_2 = 4.4$ ms, was obtained in Er^{3+}:Y$_2$SiO$_5$[20], and several hours of spin coherence lifetime have been reported in Eu^{3+}:Y$_2$SiO$_5$[21]. These attractive properties, unique in the solid state, allow RE doped crystals to be used as quantum light-matter interfaces, as shown in recent reports on quantum memories and optical to microwave transducers[22–25].

2

Despite the outstanding demonstrations reported in macroscopic crystals, RE nanoparticles offer key advantages. Indeed, these systems can be placed in an optical micro- or nano-cavity with high quality factor and low mode volume. This enables efficient single ion readout,[26,27] as well as stronger light-matter coupling, which could lead to scalable quantum processors and high fidelity memories for quantum networks[19,28,29]. Nonetheless, a major challenge is the obtention of high-quality nano-materials with long optical and spin coherence lifetimes. In this sense, Eu^{3+} doped Y_2O_3 is a particularly interesting candidate. Firstly, Eu^{3+} dopants can occupy a low symmetry site in the crystal lattice (C_2). This is favourable for the Eu^{3+}: $^7F_0 \rightarrow {}^5D_0$ electic dipole transition to be strong. Secondly, Y_2O_3 presents low nuclear spin density. This limits decoherence related to fluctuating magnetic fields in the host (due to spin-lattice relaxation and flip-flop), an important requirement for achieving narrow homogeneous linewidths. Finally, in contrast to other RE materials,[27,30–32] Eu^{3+} doped Y_2O_3 nanoparticles presenting narrow size distribution, bulk-like optical absorption and emission features and remarkable optical and spin coherence properties can be obtained by chemical synthesis[33–35]. Our previous studies on Eu^{3+}:Y_2O_3 nanoparticles synthesized by homogeneous precipitation demonstrated an optical homogeneous linewidth of 45 kHz (T_2 = 7.5 μs) for the Eu^{3+}: $^7F_0 \rightarrow {}^5D_0$ transition at 580 nm in 400-nm-diameter particles[34]. Spin homogeneous linewidth down to 40 Hz (T_2 = 8.1 ms) has also been recently reported[35]. These results are comparable to values observed in some Eu^{3+}:Y_2O_3 bulk crystals and transparent ceramics[36–40]. Still, optical micro-cavities require low scattering losses in order to reach large cavity-ion coupling. Particles significantly smaller than the optical wavelength are therefore necessary, as the scattering losses scale as the sixth power of the particle size[28].

Here, we propose wet chemical etching as a new approach to obtain well-dispersed and sub-wavelength RE doped Y_2O_3 nanoparticles with narrow homogeneous linewidths. Although the homogeneous precipitation method allows for morphology and size distribution

control, the Y_2O_3 phase forms after calcination of the precipitated yttrium carbonate precursors ($Y(OH)CO_3 \cdot x\ H_2O$, YOC), and, it was shown that high calcination temperature ($\sim 1200\ °C$) was required to cure defects and ensure good optical performance.[33,34] This sets a limit for the minimum particle size which can be obtained by this method since avoiding agglomeration and aggregation after calcination is very challenging below a certain particle diameter. Thus, our approach consists of synthesizing optimized Y_2O_3 particles with average size in the 400 nm - 500 nm range, and then applying chemical etching to achieve a controlled size reduction with low dispersion. This allows obtaining and selecting particles with appropriate size with respect to the optical micro- or nano-cavity characteristics, like the operating wavelength and targeted quality factor. The etching mechanism and the optical coherence performance at 580 nm of Eu^{3+}:Y_2O_3 etched particles were analyzed and are here discussed. Homogeneous linewidth broadening as low as 10 kHz was measured for 150 nm etched nanoparticles starting from 430 nm initial nanoparticles. The corresponding coherence lifetimes, 9.3 μs and 12.5 μs, are the longest ever reported for any nanoparticles. The results suggest that chemical etching is a promising way to obtain RE doped particles of sub-wavelength size, suitable for nanoscale quantum hardware architectures.

2 Results and discussion

2.1 Structural characterizations and etching mechanisms

Several series of Eu^{3+} doped Y_2O_3 nanoparticles were synthesized by homogenous precipitation, calcined at 1200 °C, and subsequently etched in acetic acid solutions of 50 wt.% acid content (8.53 mol L^{-1}), see Methods. A weak acid (pKa = 4.76 at 25 °C) was chosen for low etching rates, allowing control over the size reduction process. Fig. 1 shows the evolution of the particle size distribution and morphology as a function of etching time. The initial Eu^{3+}:Y_2O_3 nanoparticles exhibit spherical, well-dispersed morphology and particle size of 450 $\pm$ 56 nm according to log-normal fit. As observed, when etching time increases

4

from 1 to 5 hours, the nanoparticles turn to be gradually smaller and their shape changes, as evidenced by the appearance of sharp edges and facets. It can be noted that the size distribution of the etched particles stays comparable to that of the initial particles, slighly broadening after 4 hours etching (Fig. 1 **d** and **e**). Inductively coupled plasma atomic emission spectroscopy (ICP-AES) was used to determine the mass loss due to etching by measuring the yttrium element concentration in the acid solution after removing the etched particles. In Fig. 2, the ICP-AES results are compared to the expected mass loss based on the progressive size reduction observed in Fig. 1. This simple model assumes that the nanoparticles are perfectly spherical and that the total number of particles remains the same along the etching process. The mass of a single particle is then given by:

$$m = \rho V = \rho \frac{4}{3} \pi r^3 \tag{1}$$

in which V in the particle volume, r the particle radius and ρ the Y_2O_3 density. After an etching time t, the radius decreases from r_0 to a specific value r_e, and the mass being etched for each particle, Δm, can be expressed as:

$$\Delta m = \rho \Delta V_t = \rho \frac{4}{3} \pi (r_0^3 - r_e^3) \tag{2}$$

Then, the relative mass loss per particle just depends on the initial and final particle radii as:

$$\frac{\Delta m}{m_0} = \frac{r_0^3 - r_e^3}{r_0^3} \tag{3}$$

For an ensemble of particles with total mass $M = \sum_i m_i$ and a distribution of initial and final radii $r_{0,i}$ and $r_{e,i}$, eq. 3 becomes:

$$\frac{\Delta M}{M_0} = \frac{\sum_i (m_{0,i} - m_{e,i})}{\sum_i m_{0,i}} = \frac{\sum_i (r_{0,i}^3 - r_{e,i}^3)}{\sum_i r_{0,i}^3} \tag{4}$$
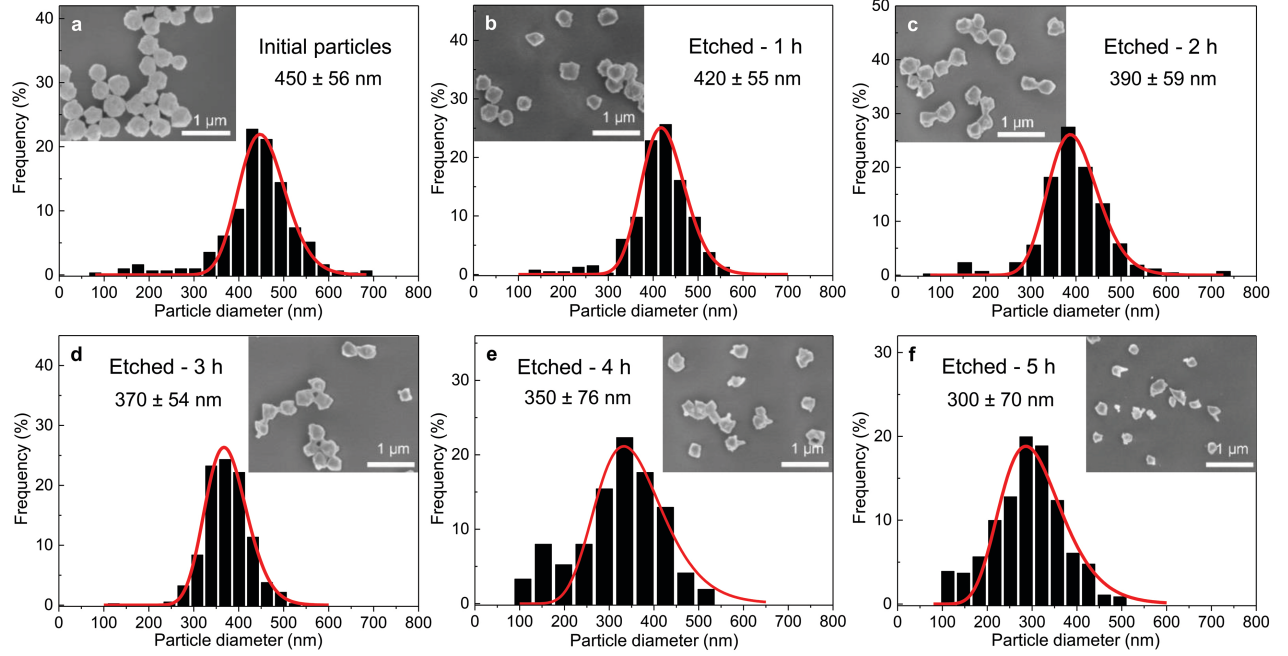
5

Figure 1: Scanning electron microscopy (SEM) micrographs and size distributions of the initial and etched Eu^{3+}:Y_2O_3 nanoparticles for etching times increasing from 1 to 5 hours (etching temperature T=50 °C).
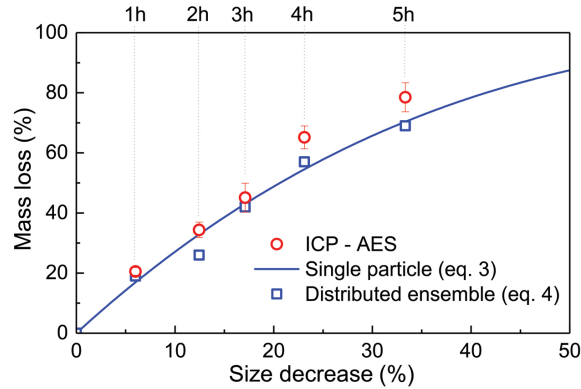

Figure 2: Relative mass loss due to etching as a function of the relative particle size decrease, $(r_0 - r_e)/r_0$, with r_0= 225 nm (initial particles) and r_e the average radius of the etched particles for different etching times, e.g. r_0= 150 nm for $t = 5$ h (Fig. 1). The experimental ICP-AES results (red dots) are compared to the mass loss expected from the size reduction model (eqs. 3 and 4) for a single average particle (line) and an ensemble of 1000 particles distributed in size as in Fig. 1 (blue squares).

6

As displayed in Fig. 2, the mass loss trend measured by ICP-AES is quite well described by eqs. 3 and 4. However, a closer insight into the etched particles inner structure indicates that this model, just considering an isotropic volume reduction of the particles, does not provide an accurate description of the etching mechanism taking place. For gaining understanding, it is important to take into account that the initial Eu^{3+}:Y_2O_3 particles are polycrystalline. Thus, they are made of multiple crystalline grains with average sizes ranging from $\approx$ 100 to 120 nm (Fig. 3). Interestingly, X-ray diffraction (XRD) analysis reveals that the etching process does not lead to a noticeable reduction of the grain size nor increases the grain size dispersion (Fig. 3). This is the case even when the average particle size after etching is close to the grain size itself (e.g. $\sim$ 150 nm). Moreover, it is evidenced in Fig. 4 that etching preferentially occurs at grain boundaries, leading to the detachment of small crystal grains as it proceeds (red arrows). Similarly, a selective etching of grain boundaries over grains has been previously reported in semiconductors as polycrystalline silicon[41]. This suggests that the mass loss shown in Fig. 2 is mainly due to these isolated grains, which once detached are etched in a rather short time. This sequential mechanism, depicted in Fig. 5, can indeed explain the morphological changes observed in Fig. 1, the constant grain size, as well as the slight increase in size distribution for the longer etching times because each particle contains less and less grains (Fig. 3).

Based on the previous conclusions, we redefined the size reduction model by taking into account the polycrystalline nature of the particles, considering an average grain diameter of 116 ± 8 nm (Fig. 3 **b**). The mass of a single particle then becomes:

$$m = n_g \times \rho V_g = n_g \times \rho \frac{4}{3} \pi r_g^3 \tag{5}$$

in which V_g is the volume of a single crystalline grain, n_g is the number of grains in the particle and r_g the grain radius. The relative mass loss per particle is then given by:
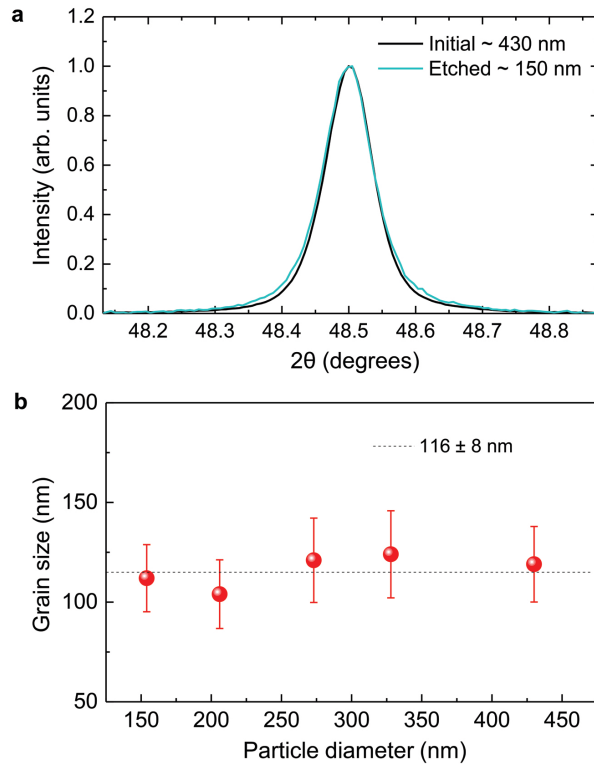
7

Figure 3: XRD investigation. **a.** Normalized diffraction peak for initial and etched particles with average sizes of 430 and 150 nm respectively. **b.** Grain size as a function of particle size. The dotted line is a guide to the eye.
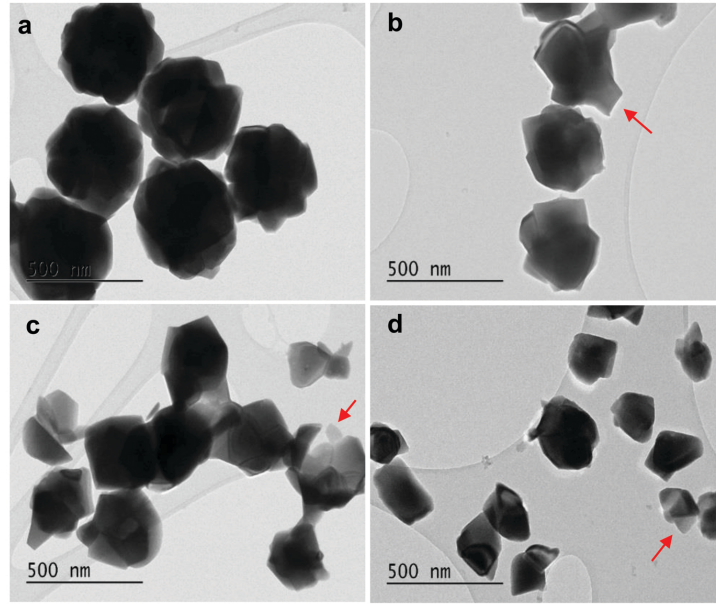
Figure 4: TEM analysis. **a.** Initial particles. **b.** 400 nm particles obtained after 2 hours etching (T=50 °C). **c.** 340 nm particles after 5 hours etching (T=50 °C). **d.** 200 nm particles obtained after 2 hours etching (T=70 °C). The temperature dependence of the etching process is later discussed in the text.
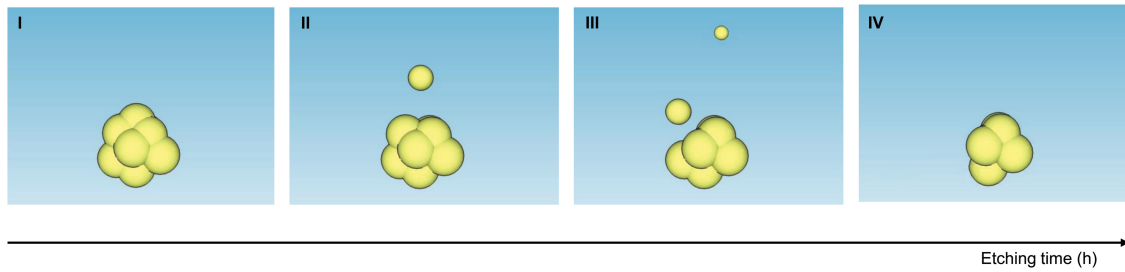

Etching time (h)

Figure 5: Schematic description of the etching process in polycrystalline Y_2O_3 nanoparticles. The acid solution preferentially attacks grain boundaries provoking crystalline grains to be progressively detached and subsequently rapidly etched, leading to an effective particle size reduction.

9

$$\frac{\Delta m}{m_0} = \frac{n_0 - n_e}{n_0} \tag{6}$$

where n_0 is the number of grains in the initial particle and n_e the number of grains in the final etched particle. By using eq. 6, the number of grains lost $(n_0 - n_e)$, i.e. detached and then fully etched, can be determined as a function of etching time from the experimental mass loss meaused by ICP-AES (Fig. 2). The result is shown in Fig. 6 **a**. A linear etching rate is found, equal to ~ 9 grains h^{-1}, or equivalently, 7.6×10^6 nm^3 h^{-1} at $T = 50$ °C. This result appears consistent with experimental evidences: at the rate found, the initial particles ($\sim$450 nm) should be completely etched after approximately 6.5 hours (Fig. 6 **b**). This was indeed observed since no particles could be collected after 6 hours of etching. It also implies that single crystalline grains are fully etched in less than 7 minutes, therefore contributing to the mass loss shortly after being isolated from the particles. The temperature dependence of the etching rate, $R(T)$, was also investigated by monitoring the particle size decrease as a function of etching temperature for a fixed etching time t. Thus, $R(T)$ was estimated as:

$$R(T) = \frac{4}{3}\pi \frac{r_0^3 - r_{e,T}^3}{t} \tag{7}$$

in which t was set equal to 2 hours, r_0=225 nm and $r_{e,T}$ is the average radius of the etched particles for different etching temperatures (Fig. 6 **c**). As displayed in Fig. 6 **d**, $R(T)$ follows the law:

$$R(T) \propto e^{-\frac{E_A}{k_B T}} \tag{8}$$

where k_B is the Boltzmann constant and E_A the activation energy, here found equal to 0.52 eV or 50.2 kJ mol^{-1} (Fig. 6 **d**). This value corresponds to a surface-reaction-limited etching process[42]. In conclusion, it is demonstrated that a controlled size reduction of the initial Eu^{3+}:Y$_2$O$_3$ particles is possible by accurately tuning etching time and temperature. The latter could be decreased to obtain particules smaller than 150 nm in a longer time and
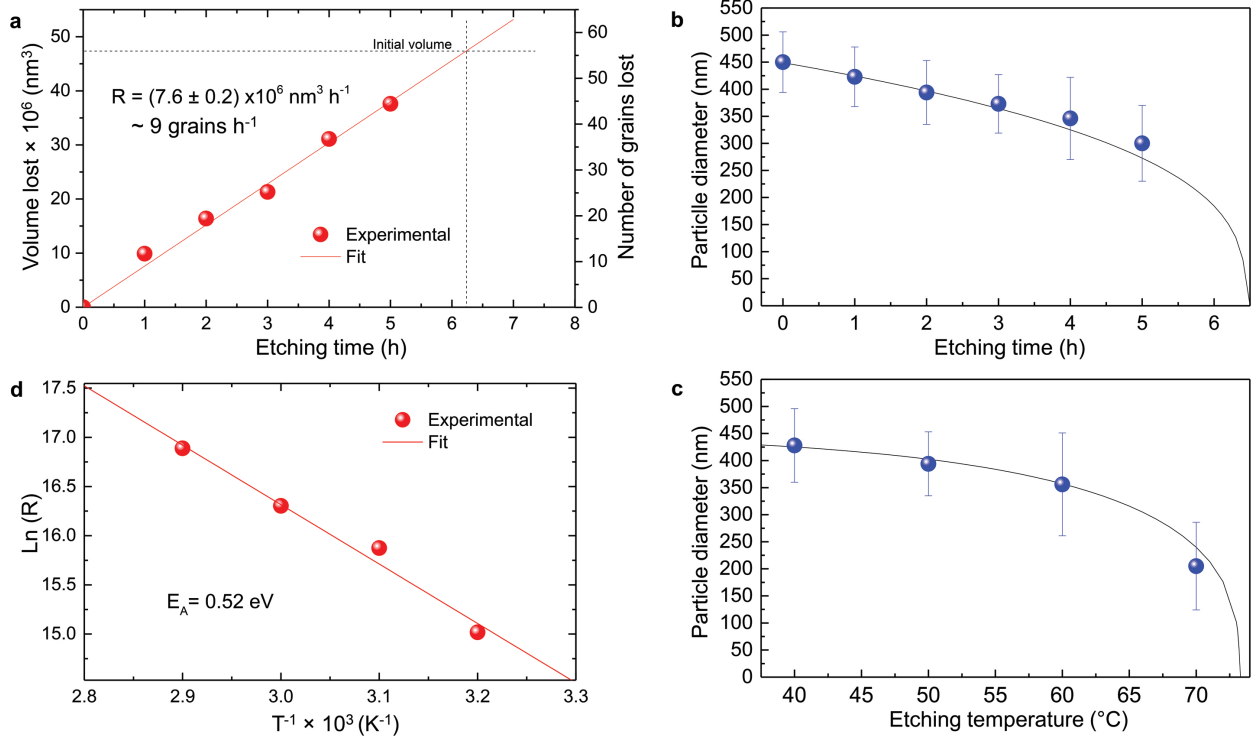
therefore with more accuracy.

Figure 6: Particle size evolution with etching time and temperature. **a.** Volume lost as a function of etching time and corresponding etching rate. **b.** Particle size decrease as a function of etching time with T = 50 °C (dots) compared to the particle size evolution expected from a rate of 7.6×10^6 nm^3 h^{-1} (line). **c.** Particle size decrease as a function of etching temperature with a fixed etching time of 2 h (dots) compared to the particle size evolution with an activation energy E_A=0.52 eV (line). **d.** $\ln(R)$ versus T^{-1} showing a linear dependence from which E_A can be calculated (eq. 8).

2.2 High resolution and coherent spectroscopy

The inhomogeneous broadening, Γ_{inh}, of initial and etched particles was recorded at low temperature ($\sim$10 K) by monitoring the $^5D_0 \rightarrow ^7F_0$ emission intensity while scanning a narrow-linewidth single frequency laser through the $^5D_0$-$^7F_0$ transition (see Methods). The initial particles showed Γ_{inh} values around 11 GHz, as expected for particles annealed at 1200 °C[33]. After etching, a clear broadening was observed in all measured samples, as in the example shown in Fig. 7. The initial and etched particles lineshapes could be described by

11

Lorentzian functions, which denotes point defects as the source of inhomogeneous broadening.[43] In non-etched particles, broadening is dominated by Eu^{3+} ions themselves, highlighting the low content of other defects in these materials[33]. Substitution of Y^{3+} by Eu^{3+} induces strain in the crystalline matrix and therefore broadening because of their different atomic radii: $r_{Eu} = 0.950$ Å, $r_Y = 0.892$ Å[44]. Upon etching, strain is not expected to change in the crystalline grains as their size is not noticeably changed during the process, as discussed in the previous section. We therefore attribute the additional broadening observed in etched particles to an increase in point defects at the surface of the crystalline grains, in agreement with the Lorentzian lineshape of the transition.
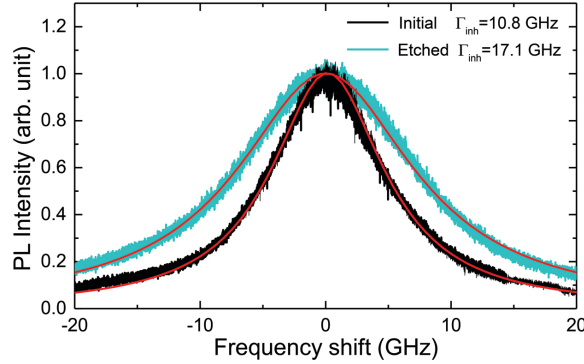

Figure 7: Inhomogeneous broadenin (Γ_{inh}) of the $^7F_0 \rightarrow ^5D_0$ optical transitions in initial (black) and etched (green) nanoparticles with average sizes of 450 and 200 nm respectively. Linewidths were estimated by Lorentzian fit.

In order to determine the impact of etching on the optical coherence of the particles we measured optical coherence lifetimes in a series of etched nanoparticles. Starting from an initial size of 430 nm, the smallest particles had an average diameter of 150 nm after etching. Coherence lifetimes T_2 and homogeneous linewidths $\Gamma_h = (\pi T_2)^{-1}$ were obtained from 2 pulse photon echo measurements[34,38] at temperatures of 1.4 ± 0.1 K (see Methods). As shown in Fig. 8 **a**, they could be fitted by a single exponential, as previously observed in other nanocrystals[38]. All measured homogeneous linewidths were below 100 kHz and the broadening attributed to etching ($\Gamma_{h,etched} - \Gamma_{h,initial}$), did not show a clear dependence on particle size as displayed in Fig. 8 **b**. In particular, the smallest particles homogeneous

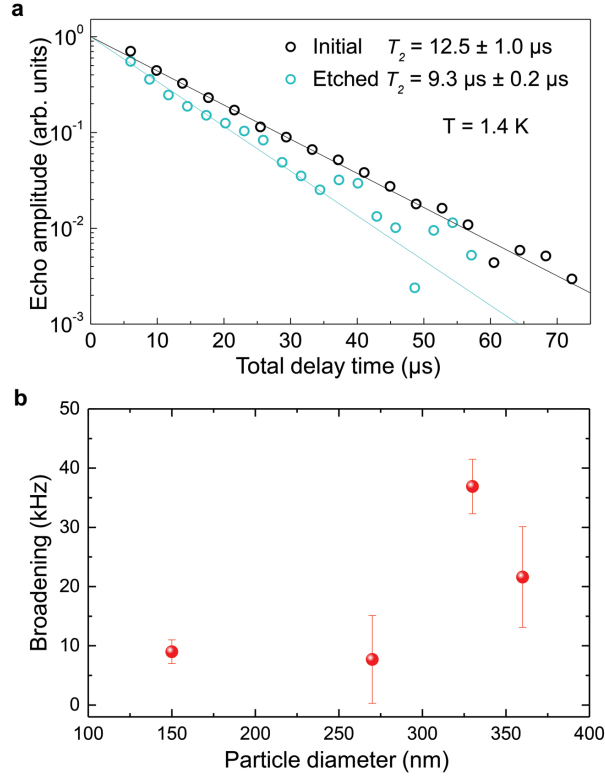Figure 8: Optical coherence lifetimes and homogenous broadening. **a** Photon echo decays for inital and etched nanoparticles at 1.4 K with average sizes of 430 and 150 nm respectively. T_2 values were derived by single exponential fit to the decay data. **b** Additional broadening due to etching as a function of the particles size. Error bars represent $\pm$ 1 standard deviation from several measurements.

linewidth was broadened by only 10 kHz compared to the initial particles. In a previous study, we attributed the main contributions to Eu^{3+} homogeneous linewidth in nanoparticles to fluctuations due to residual disorder and surface charges.[34] In all likelihood, the additional broadening induced by etching results from surface modifications (Fig. 4). Since the broadening is only weakly dependent on the particle size, it seems probable that it occurs at the crystalline grain level, whose size does not change with etching (Fig. 3). It could be explained by an increase in dynamical disorder induced by etching, which also creates static disorder as shown by the increase in Γ_{inh}. Surface charges could also increase after etching due for example to the creation of dangling bonds. Further studies involving temperature dependence of Γ_{h} and 3-pulse echoes decays could help clarify this point.[34,39]

These results demonstrate that wet chemical etching can be very useful to reduce particle size while maintaining very narrow homogeneous linewidths. For the smallest particles, we are able to decrease particle size by 65%, from 430 nm to 150 nm, (96% reduction in volume), while obtaining $\Gamma_{\mathrm{h}} = 34.2$ kHz, an unmatched value for any nanoparticle to the best of our knowledge. The significance of this linewidth can be illustrated by comparing it with the interactions used to implement quantum gates in rare earth doped crystals[45]. Based on Eu^{3+} optical Stark coefficients, electric dipole-dipole interactions will induce frequency shifts equal to Γ_{h}, i.e. 34.2 kHz, for ions separated by about 10 nm.[34] In the 150 nm particles, the average distance between Eu^{3+} ions in the C_2 site for 0.3% doped Y_2O_3 particles is 3.2 nm, whereas a single particle contains about 10^5 Eu^{3+} ions. This suggests that a large fraction of ions could interact strongly enough to explore Eu^{3+}-Eu^{3+} interactions and 2-qubit gates in a single particle that could be furthermore coupled in a medium finesse fiber micro-cavity.

3   Conclusion

In conclusion, we have found that chemical etching can be used for etching Eu^{3+}:Y_2O_3 oxide polycrystalline nanoparticles at controlled rates. The particles size can be decreased from initial large particles in the 400-500 nm range to much smaller ones (i.e. 150 nm) with a narrow distribution, good dispersion and without obvious changes on the single crystallite size. Based on imaging and structural analysis we propose an etching mechanism by acetic acid that tends to open the grain boundaries of the polycrystalline nanoparticles, detaching single crystalline grains and reducing the density and effective size of the particles. Furthermore, we demonstrate that chemical etching has a limited impact on optical performance of the nanoparticles, leading to homogeneous broadenings below 40 kHz for particles between 360 and 150 nm. Moreover, the coherence times of 12.5 μs (Γ_h = 25.5 kHz) for 430 nm initial particles and 9.3 μs (Γ_h = 34.2 kHz) for 150 nm etched nanoparticles observed at 1.4 K, are the longest optical coherence times ever reported for nanoparticles. Our results demonstrate that chemical etching is a promising way to synthesize RE:Y_2O_3 nanoparticles suitable for coupling with optical micro-cavities and with long coherence lifetimes, opening the way to efficient nanoscale quantum memories and processors.

4   Methods

The initial 0.3 at.% Eu^{3+}:Y_2O_3 nanoparticles were synthesized by homogeneous precipitation with a calcination temperature of 1200 °C. The detailed technological route has been described in previous work[33]. The etching agent used in the study was glacial acetic acid (CH_3COOH, original concentration of 100 wt.%, with density 1.05 g.cm^{-3}). Chemical etching experiments were carried out by mixing Eu^{3+}:Y_2O_3 nanoparticles with fresh acid solutions (50 wt.% prepared with deionized water). To ensure homogeneous temperature in the acid solution, etching was done under water-bath, with continuous magnetic agitation. After chemical etching, the nanoparticles were collected by centrifugation and washed sev-

eral times with deionized water and absolute ethanol to remove the byproducts. The final etched powders were obtained after drying at 80 °C for 24 h. A post microwave treatment under oxygen plasma was performed to remove impurities. In order to clarify the effect of various etching conditions on the structures of the nanoparticles, etching time from 1 to 5 h, water-bath temperature from 40 to 70 °C and acetic acid concentration from 40 to 70 wt.% were investigated. No dependence on the acetic acid content was found, while the effect of etching time and temperature is discussed in the manuscript.

The morphology of the initial and etched particles was observed with scanning electron microscopy (SEM, Zeiss Leo1530) and transmission electron microscopy (TEM, JEOL-JEM-100CXI) operating at 100 kV. Particle size and distribution were calculated based on at least 300 nanoparticles by Image J software. XRD measurements were performed on a Panalytical XPert Pro diffractometer with an incident beam Ge monochromator. Crystallite or single grain sizes were determined using the FWHM of 4 different diffraction peaks and the Scherrer formula. The mass loss due to etching was derived from the concentration of yttrium in the etched solutions measured by inductively coupled plasma atomic emission spectrometry (ICP-AES, ThermalFisher icp 6000)[46,47].

Measurements of the inhomogeneous and homogeneous linewidths were carried out on selected samples based on the size obtained for the etched particles. The samples in form of powders were placed in a helium bath cryostat (Janis SVT-200) and maintained in a copper holder between two glass plates. The detection was carried out by collecting light scattered through the sample as explained in previous works[34,38]. The inhomogeneous linewidth (Γ_h) of the Eu^{3+}: $^7F_0 \rightarrow ^5D_0$ transition was recorded at approximately 10 K, by fluorescence excitation using a CW dye ring laser (Sirah Matisse DS, 200 kHz linewidth) pumped by a Coherent Verdi G10 laser. A long-pass filter (600 nm cut-off wavelength) was placed in front of the detector (APD Thorlabs 110 A/M) to reject the excitation light. Homogeneous linewidths Γ_h were determined from coherence lifetimes (T_2) measured by two pulse photon

echo experiments at the center of the $^7F_0 \rightarrow ^5D_0$ (580.88 nm in vacuum) transition at 1.4 K . The length of the exciting and rephasing pulses in the sequence was 1 and 1.5 μs respectively.

Acknowledgement

References

(1) Weber, M. J. *Handbook on the Physics and Chemistry of Rare Earths*; Non-Metallic Compounds - II; Elsevier, 1979; Vol. 4; pp 275–315.

(2) Digonnet, M. J. F. *Rare-Earth-Doped Fiber Lasers and Amplifiers, Revised and Expanded*; CRC Press, 2001; Google-Books-ID: nTxd78tikA0C.

(3) Ronda, C. R.; Jüstel, T.; Nikol, H. Rare earth phosphors: fundamentals and applications. *J. Alloys Compd.* **1998**, *275-277*, 669–676.

(4) Rowan, B. C.; Wilson, L. R.; Richards, B. S. Advanced Material Concepts for Luminescent Solar Concentrators. *IEEE J. Sel. Top. Quantum. Electron.* **2008**, *14*, 1312–1322.

(5) Bouzigues, C.; Gacoin, T.; Alexandrou, A. Biological Applications of Rare-Earth Based Nanoparticles. *ACS Nano* **2011**, *5*, 8488–8505.

(6) Abdesselem, M.; Schoeffel, M.; Maurin, I.; Ramodiharilafy, R.; Autret, G.; Clńment, O.; Tharaux, P.-L.; Boilot, J.-P.; Gacoin, T.; Bouzigues, C.; Alexandrou, A. Multifunctional Rare-Earth Vanadate Nanoparticles: Luminescent Labels, Oxidant Sensors, and MRI Contrast Agents. *ACS Nano* **2014**, *8*, 11126–11137.

(7) Sinha, G.; Patra, A. Generation of green, red and white light from rare-earth doped Ga$_2$O$_3$ nanoparticles. *Chem. Phys. Lett.* **2009**, *473*, 151–154.

(8) Kim, W. J.; Nyk, M.; Prasad, P. N. Color-coded multilayer photopatterned microstructures using lanthanide (III) ion co-doped NaYF$_4$ nanoparticles with upconversion luminescence for possible applications in security. *Nanotechnology* **2009**, *20*, 185301.

(9) Thiel, C. W.; Böttger, T.; Cone, R. L. Rare-earth-doped materials for applications in quantum information storage and signal processing. *J. Lumin.* **2011**, *131*, 353–361.

(10) Tittel, W.; Afzelius, M.; Chaneliere, T.; Cone, R. L.; Kröll, S.; Moiseev, S. A.; Sellars, M. Photon-echo quantum memory in solid state systems. *Laser & Photon. Rev.* **2010**, *4*, 244–267.

(11) Goldner, P.; Ferrier, A.; Guillot-Noël, O. Rare Earth-Doped Crystals for Quantum Information Processing. *Handbook on the Physics and Chemistry of Rare Earths* **2015**, *46*, 1–78.

(12) Kunkel, N.; Goldner, P. Recent Advances in Rare Earth Doped Inorganic Crystalline Materials for Quantum Information Processing. *Z. anorg. allg. Chem.* **2018**, *644*, 66–76.

(13) Welinski, S.; Ferrier, A.; Afzelius, M.; Goldner, P. High-resolution optical spectroscopy and magnetic properties of Yb^{3+} in Y$_2$SiO$_5$. *Phys. Rev. B* **2016**, *94*, 155116.

(14) Equall, R. W.; Sun, Y.; Cone, R. L.; Macfarlane, R. M. Ultraslow optical dephasing in Eu^{3+}:Y$_2$SiO$_5$. *Phys. Rev. Lett.* **1994**, *72*, 2179–2182.

(15) Böttger, T.; Thiel, C. W.; Cone, R. L.; Sun, Y. Effects of magnetic field orientation on optical decoherence in Er^{3+}:Y$_2$SiO$_5$. *Phys. Rev. B* **2009**, *79*, 115104.

(16) Usmani, I.; Afzelius, M.; de Riedmatten, H.; Gisin, N. Mapping multiple photonic qubits into and out of one solid-state atomic ensemble. *Nat. Commun.* **2010**, *1*, 12.

(17) Equall, R. W.; Cone, R. L.; Macfarlane, R. M. Homogeneous broadening and hyperfine structure of optical transitions in Pr^{3+}:Y_2SiO_5. *Phys. Rev. B* **1995**, *52*, 3963–3969.

(18) Louchet, A.; Habib, J. S.; Crozatier, V.; Lorgeré, I.; Goldfarb, F.; Bretenaker, F.; Le Gouët, J.-L.; Guillot-Noël, O.; Goldner, P. Branching ratio measurement of a Λ system in Tm^{3+}:YAG under magnetic field. *Phys. Rev. B* **2007**, *75*, arXiv: quant-ph/0606048.

(19) Zhong, T.; Kindem, J. M.; Bartholomew, J. G.; Rochman, J.; Craiciu, I.; Miyazono, E.; Bettinelli, M.; Cavalli, E.; Verma, V.; Nam, S. W.; Marsili, F.; Shaw, M. D.; Beyer, A. D.; Faraon, A. Nanophotonic rare-earth quantum memory with optically controlled retrieval. *Science* **2017**, *357*, 1392–1395.

(20) Böttger, T.; Thiel, C. W.; Sun, Y.; Cone, R. L. Optical decoherence and spectral diffusion at 1.5 μm in Er^{3+}:Y_2SiO_5 versus magnetic field, temperature, and Er^{3+} concentration. *Phys. Rev. B* **2006**, *73*, 075101.

(21) Zhong, M.; Hedges, M. P.; Ahlefeldt, R. L.; Bartholomew, J. G.; Beavan, S. E.; Wittig, S. M.; Longdell, J. J.; Sellars, M. J. Optically addressable nuclear spins in a solid with a six-hour coherence time. *Nature* **2015**, *517*, 177.

(22) Bussières, F.; Clausen, C.; Tiranov, A.; Korzh, B.; Verma, V. B.; Nam, S. W.; Marsili, F.; Ferrier, A.; Goldner, P.; Herrmann, H.; Silberhorn, C.; Sohler, W.; Afzelius, M.; Gisin, N. Quantum teleportation from a telecom-wavelength photon to a solid-state quantum memory. *Nat. Photonics* **2014**, *8*, 775.

(23) Saglamyurek, E.; Jin, J.; Verma, V. B.; Shaw, M. D.; Marsili, F.; Nam, S. W.; Oblak, D.; Tittel, W. Quantum storage of entangled telecom-wavelength photons in an erbium-doped optical fibre. *Nat. Photonics* **2015**, *9*, 83.

(24) Maring, N.; Farrera, P.; Kutluer, K.; Mazzera, M.; Heinze, G.; de Riedmatten, H.

Photonic quantum state transfer between a cold atomic gas and a crystal. *Nature* **2017**, *551*, 485.

(25) Williamson, L. A.; Chen, Y.-H.; Longdell, J. J. Magneto-Optic Modulator with Unit Quantum Efficiency. *Phys. Rev. Lett.* **2014**, *113*, 203601.

(26) Kolesov, R.; Xia, K.; Reuter, R.; Stöhr, R.; Zappe, A.; Meijer, J.; Hemmer, P. R.; Wrachtrup, J. Optical detection of a single rare-earth ion in a crystal. *Nat. Commun.* **2012**, *3*, 1029.

(27) Utikal, T.; Eichhammer, E.; Petersen, L.; Renn, A.; Götzinger, S.; Sandoghdar, V. Spectroscopic detection and state preparation of a single praseodymium ion in a crystal. *Nat. Commun.* **2014**, *5*, 3627.

(28) Casabone, B.; Benedikter, J.; Hümmer, T.; Beck, F.; de Oliveira Lima, K.; Hänsch, T. W.; Ferrier, A.; Goldner, P.; de Riedmatten, H.; Hunger, D. Cavity-enhanced spectroscopy of a few-ion ensemble in $Eu^{3+}:Y_2O_3$. *arXiv:1802.06709* **2018**,

(29) Dibos, A.; Raha, M.; Phenicie, C.; Thompson, J. Isolating and enhancing the emission of single erbium ions using a silicon nanophotonic cavity. *arXiv:1711.10368v1* **2017**,

(30) Eichhammer, E.; Utikal, T.; Götzinger, S.; Sandoghdar, V. Spectroscopic detection of single Pr^{3+} ions on the $^3H_4-^1D_2$ transition. *New J. Phys.* **2015**, *17*, 1–7.

(31) Lutz, T.; Veissier, L.; Thiel, C. W.; Woodburn, P. J. T.; Cone, R. L.; Barclay, P. E.; Tittel, W. Effects of fabrication methods on spin relaxation and crystallite quality in Tm-doped powders studied using spectral hole burning. *Sci. Technol. Adv. Mater.* **2016**, *17*, 63–70.

(32) Lutz, T.; Veissier, L.; Thiel, C. W.; Woodburn, P. J. T.; Cone, R. L.; Barclay, P. E.; Tittel, W. Effects of mechanical processing and annealing on optical coherence properties of $Er^{3+}:LiNbO_3$ powders. *J. Lumin.* **2017**, *191*, 2–12.

(33) de Oliveira Lima, K.; Rocha Gonçalves, R.; Giaume, D.; Ferrier, A.; Goldner, P. Influence of defects on sub-Å optical linewidths in $Eu^{3+}:Y_2O_3$ particles. *J. Lumin.* **2015**, *168*, 276–282.

(34) Bartholomew, J. G.; Lima, K. D.; Ferrier, A.; Goldner, P. Optical Line Width Broadening Mechanisms at the 10 kHz Level in $Eu^{3+}:Y_2O_3$ Nanoparticles. *Nano Lett.* **2017**, *17*, 778–787.

(35) Serrano, D.; Karlsson, J.; Fossati, A.; Ferrier, A.; Goldner, P. All-optical control of long-lived nuclear spins in rare-earth doped nanoparticles. *Nature Communications* **2018**, *9*, 2127.

(36) Flinn, G. P.; Jang, K. W.; Ganem, J.; Jones, M. L.; Meltzer, R. S.; Macfarlane, R. M. Sample-dependent optical dephasing in bulk crystalline samples of $Y_2O_3:Eu^{3+}$. *Phys. Rev. B* **1994**, *49*, 5821–5827.

(37) Ferrier, A.; Thiel, C. W.; Tumino, B.; Ramirez, M. O.; Bausá, L. E.; Cone, R. L.; Ikesue, A.; Goldner, P. Narrow inhomogeneous and homogeneous optical linewidths in a rare earth doped transparent ceramic. *Phys. Rev. B* **2013**, *87*, 041102.

(38) Perrot, A.; Goldner, P.; Giaume, D.; Lovrić, M.; Andriamiadamanana, C.; Gonçalves, R. R.; Ferrier, A. Narrow optical homogeneous linewidths in rare earth doped nanocrystals. *Phys. Rev. Lett.* **2013**, *111*, 203601.

(39) Kunkel, N.; Bartholomew, J.; Welinski, S.; Ferrier, A.; Ikesue, A.; Goldner, P. Dephasing mechanisms of optical transitions in rare-earth-doped transparent ceramics. *Phys. Rev. B* **2016**, *94*.

(40) Karlsson, J.; Kunkel, N.; Ikesue, A.; Ferrier, A.; Goldner, P. Nuclear spin coherence properties of $^{151}Eu^{3+}$ and $^{153}Eu^{3+}$ in a Y_2O_3 transparent ceramic. *J. Phys.: Condens. Matter* **2017**, *29*, 125501.

(41) Yoo, S.-J.; Lee, J.; Shin, H. A new quantum dot formation process using wet etching of poly-Si along grain boundaries. Digest of Papers Microprocesses and Nanotechnology 2000. 2000 International Microprocesses and Nanotechnology Conference (IEEE Cat. No.00EX387). 2000; pp 248–249.

(42) Tan, S.; Boudreau, R.; Reed, M. L. Measurement of 111 silicon anisotropic etching activation energy. Technical Digest. MEMS 2001. 14th IEEE International Conference on Micro Electro Mechanical Systems (Cat. No.01CH37090). 2001; pp 139–142.

(43) Stoneham, A. M. Shapes of inhomogeneously broadened resonance lines in solids. *Rev. Mod. Phys.* **1969**, *41*, 82.

(44) Shannon, R. D.; Prewitt, C. T. Effective ionic radii in oxides and fluorides. *Acta Cryst. B* **1969**, *25*, 925–946.

(45) Walther, A.; Rippe, L.; Yan, Y.; Karlsson, J.; Serrano, D.; Nilsson, A. N.; Bengtsson, S.; Kröll, S. High-fidelity readout scheme for rare-earth solid-state quantum computing. *Phys. Rev. A* **2015**, *92*, 022319.

(46) Atanassova, D.; Stefanova, V.; Russeva, E. Co-precipitative pre-concentration with sodium diethyldithiocarbamate and ICP-AES determination of Se, Cu, Pb, Zn, Fe, Co, Ni, Mn, Cr and Cd in water. *Talanta* **1998**, *47*, 1237–1243.

(47) Ferreira, S. L. C.; de Brito, C. F.; Dantas, A. F.; Lopo de Araujo, N. M.; Costa, A. C. S. Nickel determination in saline matrices by ICP-AES after sorption on Amberlite XAD-2 loaded with PAN. *Talanta* **1999**, *48*, 1173–1177.

Graphical TOC Entry